Journal of *Marine Science and Engineering*

MDPI

Article

A Mainlobe Interference Suppression Method for Small Hydrophone Arrays

Wenbo Wang [1], Ye Li [1,*], Luwen Meng [2], Tongsheng Shen [2] and Dexin Zhao [2,*]

[1] Science and Technology on Underwater Vehicle Laboratory, Harbin Engineering University, Harbin 150001, China
[2] National Innovation Institute of Defense Technology, Chinese Academy of Military Science, Beijing 100071, China
* Correspondence: liye@hrbeu.edu.cn (Y.L.); zdx_3s@163.com (D.Z.)

Abstract

In order to solve the problem of mainlobe interference in small hydroacoustic array signal processing, this paper proposes a beamforming method based on the high-resolution direction of arrival (DOA) estimation and interference coherence matrix (ICM) reconstruction. The DOA estimation is first performed using an improved sparse iterative covariance-based (SPICE) method, unaffected by the coherent signal, and it can provide highly accurate DOA estimation for multiple targets. The fitted signal energy distribution obtained from the SPICE is then utilized for the reconstruction of the signal coherence matrix. The reconstructed ICM matrix is used to construct a blocking masking matrix and an eigen-projection matrix to suppress the mainlobe interference signal. Compared with existing methods, the method in this paper possesses better mainlobe interference suppression ability. Within the mainlobe interference interval angle of 3° to 13.5° from the signal of interest (SOI) based on eight-element uniform linear arrays, the method in this paper can enhance the signal-to-interference ratio (SIR) by about 15.59 dB on average compared with the interference-free suppression of conventional beamforming (CBF) and outperforms the other interference suppression methods simultaneously. Simulations and experiments demonstrate the effectiveness of this method in mainlobe interference scenarios.

Keywords: hydroacoustic signal processing; small-size hydrophone arrays; mainlobe interference; interference suppression; adaptive beamforming

check for updates

Academic Editors: Jaehak Chung, Hojun Lee and Yongcheol Kim

Received: 20 June 2025
Revised: 12 July 2025
Accepted: 13 July 2025
Published: 16 July 2025

Citation: Wang, W.; Li, Y.; Meng, L.; Shen, T.; Zhao, D. A Mainlobe Interference Suppression Method for Small Hydrophone Arrays. *J. Mar. Sci. Eng.* **2025**, *13*, 1348. https://doi.org/10.3390/jmse13071348

Copyright: © 2025 by the authors. Licensee MDPI, Basel, Switzerland. This article is an open access article distributed under the terms and conditions of the Creative Commons Attribution (CC BY) license (https://creativecommons.org/licenses/by/4.0/).

1. Introduction

Currently, small sonar arrays are a hot research direction. Such arrays can be deployed on small underwater devices such as autonomous underwater vehicles (AUVs). They can provide a low-cost detection solution for underwater navigation [1], underwater exploration [2], environmental monitoring [3–5], marine life observation [6], target tracking [7,8], and other missions. The array can be mounted in two ways: mounted [9] and towed [10]. Our research objective is to provide an interference suppression and acoustic signal enhancement solution based on mounted small passive arrays for target recognition [11] and data acquisition, focusing on multi-target and strong mainlobe interference problems.

The performance of traditional array signal processing algorithms is highly dependent on array geometry parameters, especially array size and number of array elements. Unfortunately, when using non-ideal array geometries, such as small arrays mounted due

to the size constraints of underwater vehicles, the problem of excessive mainlobe width occurs [12]. The lower the frequency of the hydroacoustic signal, the longer the propagation distance, and the more array elements, the more excellent the directivity. With a fixed platform volume, the more array elements are arranged, the smaller the spacing between the array elements becomes [13]. This means that the number of small array elements is usually small in order to ensure effective detection range, which in turn leads to the problem of large mainlobe width. With a small number of array elements, when the angle between the SOI and the interference is so small as to be in the mainlobe at the same time, it leads to a catastrophic degradation of the beamforming effect.

With the significant development of adaptive beamformers in radar, navigation, radio astronomy, and microphone array speech processing, super-resolution beamforming methods applicable to small arrays are emerging, such as SPICE [14–16], sparse Bayesian learning (SBL) [17,18] and so on. However, at present, in the field of hydroacoustic signal processing, the focus of researchers is concentrated on the positioning accuracy of small arrays, and there needs to be more research on subsequent signal processing, especially the mainlobe interference problem that widely exists in detecting small arrays. Currently, common methods of interference suppression are blocking matrix preprocessing (BMP) [19], eigen-projection matrix preprocessing (EMP) [20–22], and interference and noise covariance matrix (INCM) methods [23]. The BMP method uses a vector of orientations to construct a dimensionality-decreasing blocking matrix to suppress mainlobe interference. The EMP method uses an eigen-projection method to construct an eigen-projection matrix to be used as the signal weights to suppress mainlobe interference. INCM methods are spatial matrix reconstruction processes that seek to eliminate the effect of the SOI components in the computation of adaptive weight vectors for suppressing interference. However, the performance of the method degrades when coherent interference is present. Reference [24] introduced the iterative adaptive approach (IAA) to eliminate the effect of coherent interference on localization. However, this method produces a large mainlobe offset in small arrays, and reduces the target gain.

In this paper, we propose a new method that avoids the drawbacks of the above methods as much as possible. We first use an improved SPICE method for high-accuracy DOA estimation, independent of coherent signals, which can provide accurate DOA estimation with super-resolution. Coherence matrix reconstruction of the interfering signal is then performed using the fitted signal energy distribution in the SPICE estimation. The reconstructed ICM matrix is used to construct an eigen-projection matrix by performing eigen-projection processing and blocking masking to suppress the mainlobe interference signal. Compared with the existing methods, the method in this paper can better suppress the mainlobe interference. Within the mainlobe interference interval angle of 3° to 13.5° from the SOI based on eight-element uniform linear arrays, the method in this paper can enhance the SIR by about 15.59 dB on average compared with the interference-free suppression of CBF and outperforms the other interference suppression methods simultaneously. Experiments demonstrate the effectiveness of this method in mainlobe interference scenarios.

The rest of this paper is organized as follows. Section 2 introduces the principle of this method and part of the formula derivation. Section 3 introduces the development of simulation experiments and shows the simulation performance of each comparison method's mainlobe interference suppression under different angle intervals, SIR inputs, and other variables. Section 4 describes the experimental setup and the performance of each method in the real environment. Section 5 discusses the advantages and disadvantages of this method. Finally, Section 6 summarizes the contribution of this work. At the end of the article, we also attach an abbreviation comparison at the end of this paper.

2. Methods

2.1. Signal Model

Consider a hydrophone array with M array elements; the number of underwater signal sources is N, and the number of snapshots captured in a finite time is T_s. Then, the received signal at a certain point in time t can be expressed as

$$\boldsymbol{y}(t) = \boldsymbol{\Phi}\boldsymbol{x}(t) + \boldsymbol{e}(t) \tag{1}$$

$$\boldsymbol{\Phi} = [a(\theta_1), a(\theta_2), \cdots, a(\theta_N)]. \tag{2}$$

The bold in the formulas denotes matrices, and y is the received signal, x is the source signal, $a(\theta_1)$ is the direction vector of θ_1 and e is the noise. Expanding on the time dimension with T_s expressed as a matrix,

$$\boldsymbol{Y} = \boldsymbol{\Phi}\boldsymbol{X} + \boldsymbol{E}. \tag{3}$$

Assuming that each signal source is uncorrelated and independent of the noise, the covariance matrix $\boldsymbol{R}$ is shown as

$$\begin{aligned} \boldsymbol{R} &= E\left\{\boldsymbol{y}(t)\boldsymbol{y}(t)^H\right\} \\ &= \sum_{n=1}^{N} p_n^x \boldsymbol{a}(\theta_n)\boldsymbol{a}(\theta_n)^H + E\left\{\boldsymbol{e}(t)\boldsymbol{e}(t)^H\right\} \\ &= \boldsymbol{\Phi}\boldsymbol{P}_x\boldsymbol{\Phi}^H + \boldsymbol{P}_e \end{aligned} \tag{4}$$

where $E\{\cdot\}$ represents the expectation operator. $\boldsymbol{y}(t)^H$ denotes the Hermite transpose of $\boldsymbol{y}(t)$, and the signal power matrix $\boldsymbol{P}_x$ and the noise power matrix $\boldsymbol{P}_e$ are respectively denoted as

$$\boldsymbol{P}_x = \begin{bmatrix} p_1^x & 0 & \cdots & 0 \\ 0 & p_2^x & \cdots & \vdots \\ \vdots & \vdots & \ddots & 0 \\ 0 & \cdots & 0 & p_N^x \end{bmatrix}, \boldsymbol{P}_e = \begin{bmatrix} \sigma_1 & 0 & \cdots & 0 \\ 0 & \sigma_2 & \cdots & \vdots \\ \vdots & \vdots & \ddots & 0 \\ 0 & \cdots & 0 & \sigma_M \end{bmatrix}. \tag{5}$$

2.2. Improved DOA Estimation Method

In this paper, high-resolution angle estimation is performed using an improved SPICE estimation method we proposed in Reference [25]. As an on-grid fitting method, the signal is imagined to fall perfectly in a set of discrete angular grids over a range of continuous directions, and the grid length is L. The angle grids can then be expressed as $\Theta = [\Theta_1, \Theta_2, \cdots, \Theta_L]$, then the covariance matrix can be expanded into the following:

$$\boldsymbol{R} = [a(\Theta_1), a(\Theta_2), \cdots, a(\Theta_L)] \begin{bmatrix} p_1 & 0 & \cdots & 0 \\ 0 & p_2 & \cdots & \vdots \\ \vdots & \vdots & \ddots & 0 \\ 0 & \cdots & 0 & p_L \end{bmatrix} \begin{bmatrix} a(\Theta_1)^H \\ a(\Theta_2)^H \\ \cdots \\ a(\Theta_L)^H \end{bmatrix} + \begin{bmatrix} \sigma_1 & 0 & \cdots & 0 \\ 0 & \sigma_2 & \cdots & \vdots \\ \vdots & \vdots & \ddots & 0 \\ 0 & \cdots & 0 & \sigma_M \end{bmatrix}. \tag{6}$$

It can be further abbreviated as

$$\boldsymbol{R} \triangleq \boldsymbol{\Psi}\tilde{\boldsymbol{P}}\boldsymbol{\Psi}^H \tag{7}$$

where

$$\boldsymbol{\Psi} = [a(\Theta_1), a(\Theta_2), \cdots, a(\Theta_L), \boldsymbol{I}_M] \triangleq [\boldsymbol{\varphi}_1, \boldsymbol{\varphi}_2, \cdots, \boldsymbol{\varphi}_L, \boldsymbol{\varphi}_{L+1}, \cdots, \boldsymbol{\varphi}_{L+M}] \tag{8}$$

$$\widetilde{\boldsymbol{P}} \triangleq \begin{bmatrix} \boldsymbol{P}_s & 0 \\ 0 & \boldsymbol{P}_e \end{bmatrix} \triangleq \begin{bmatrix} p_1 & 0 & \cdots & \cdots & \cdots & \cdots & 0 \\ 0 & p_2 & 0 & \cdots & \cdots & \cdots & \vdots \\ \vdots & 0 & \ddots & \vdots & \vdots & \vdots & \vdots \\ 0 & \cdots & \cdots & p_L & 0 & \cdots & 0 \\ 0 & \cdots & \cdots & 0 & p_{L+1} & \cdots & 0 \\ \vdots & \vdots & \vdots & \vdots & 0 & \ddots & 0 \\ 0 & \cdots & \cdots & \cdots & \cdots & \cdots & p_{L+M} \end{bmatrix}. \tag{9}$$

The $\boldsymbol{I}_M$ is the identity matrix of order M. The first L elements on the diagonal are the corresponding energy distributions of the received signals in space on the grid. According to the covariance fitting criterion [26], the minimization criterion is formed as

$$f(\boldsymbol{\Theta}, \widetilde{\boldsymbol{P}}) = \left\| \boldsymbol{R}^{-1/2} (\widehat{\boldsymbol{R}} - \boldsymbol{R}) \widehat{\boldsymbol{R}}^{-1/2} \right\|_2^2. \tag{10}$$

$\boldsymbol{R}^{-1/2}$ is used to find the Hermitian positive definite square root of $\boldsymbol{R}^{-1}$, and $\|\cdot\|_2$ denotes the L2 norm. The sample covariance is

$$\widehat{\boldsymbol{R}} = \boldsymbol{Y}\boldsymbol{Y}^H / T_s. \tag{11}$$

According to Reference [27], the minimization of the above equation is equivalent to the minimization of the following Equation (12):

$$g(\boldsymbol{\Theta}, \widetilde{\boldsymbol{P}}) = \mathrm{tr}\left(\widehat{\boldsymbol{R}}^{1/2} \boldsymbol{R}^{-1} \widehat{\boldsymbol{R}}^{1/2} \right) + \sum_{l=1}^{L+M} p_l \boldsymbol{\varphi}_l^H \widehat{\boldsymbol{R}}^{-1} \boldsymbol{\varphi}_l. \tag{12}$$

where

$$\omega_l = \boldsymbol{\varphi}_l^H \widehat{\boldsymbol{R}}^{-1} \boldsymbol{\varphi}_l / M \tag{13}$$

and ω_l is an element in $\boldsymbol{\omega}$, and the first L ω_l make up $\boldsymbol{\omega}_p$. Similarly, the latter M ω_l form $\boldsymbol{\omega}_\sigma$. Observe the noise space and the power space separately.

$$\min_{p_l \geq 0, \sigma_l \geq 0} \mathrm{tr}\left(\widehat{\boldsymbol{R}}^{1/2} \boldsymbol{R}^{-1} \widehat{\boldsymbol{R}}^{1/2} \right) + \|\boldsymbol{\omega} \widetilde{\boldsymbol{P}}\|_1 \tag{14}$$

$$\Rightarrow \min_{p_l \geq 0, \sigma_l \geq 0} \mathrm{tr}\left(\boldsymbol{B}^H \widetilde{\boldsymbol{P}}^{-1} \boldsymbol{B} \right) + \left\| \boldsymbol{\omega}_p \boldsymbol{P}_s \right\|_1 + \left\| \boldsymbol{\omega}_\sigma \boldsymbol{P}_e \right\|_1 \tag{15}$$

where $\boldsymbol{B}$ satisfies

$$\boldsymbol{B} = \begin{bmatrix} \boldsymbol{b}_p \\ \boldsymbol{b}_\sigma \end{bmatrix} = \widetilde{\boldsymbol{P}} \boldsymbol{\Psi}^H \boldsymbol{R}^{-1} \widehat{\boldsymbol{R}}^{1/2} \tag{16}$$

where $\|\cdot\|_1$ denotes L1 norm. The minimization formula for $g(\boldsymbol{\Theta}, \widetilde{\boldsymbol{P}})$ can be transformed into

$$\min_{p_l \geq 0, \sigma_l \geq 0} \operatorname{tr}\left(\widehat{\boldsymbol{R}}^{1/2} \boldsymbol{R}^{-1} \hat{\boldsymbol{R}}^{1/2}\right) + \left\|\boldsymbol{\omega}_p \boldsymbol{P}_s\right\|_1 + \left\|\boldsymbol{\omega}_\sigma \boldsymbol{P}_e\right\|_1 \tag{17}$$

$$\Rightarrow \operatorname{tr}\left(\boldsymbol{B}^H \tilde{\boldsymbol{P}}^{-1} \boldsymbol{B}\right) + \left\|\boldsymbol{\omega}_p \boldsymbol{P}_s\right\|_1 + \left\|\boldsymbol{\omega}_\sigma \boldsymbol{P}_e\right\|_2 \tag{18}$$

$$= \operatorname{tr}\left(\boldsymbol{B}^H \tilde{\boldsymbol{P}}^{-1} \boldsymbol{B}\right) + \sum_{l=1}^{L} \omega_l p_l + \left(\sum_{l=1}^{M} \omega_{L+l}^2 \sigma_l^2\right)^{1/2}. \tag{19}$$

Note that the L2 norm is introduced to the gradient descent process of Equation (19) to avoid unnecessary zeroing of the noise component by the L1 norm. Then customized weights are introduced in the noise component $k_l^{[i]}$ ($[i]$ denotes the current iteration period), and the gradient formula for the noise iteration is expressed as Equation (20).

$$\sigma_l^{[i+1]} = \sigma_l^{[i]} + k_l^{[i]} \left\| \varphi_{L+l}^H \left(\boldsymbol{R}^{[i]}\right)^{-1} \widehat{\boldsymbol{R}}^{1/2} \right\|_2^2 - k_l^{[i]} \omega_{L+l}^2 \sigma_l^{[i]} \left(\sum_{l=1}^{M} \omega_{L+l}^2 \left(\sigma_l^{[i]}\right)^2\right)^{-1/2}. \tag{20}$$

At this point, the design iteration weight $k_l^{[i]}$ is

$$k_l^{[i]} = \frac{\|\boldsymbol{\omega}_\sigma \boldsymbol{b}_\sigma\|_2^2 |\boldsymbol{b}_l|^{1/2} - \delta \sigma_l^{[i]} \omega_{L+l}^{1/2}}{\delta \omega_{L+l}^{1/2} \left(\omega_{L+l}^2 \sigma_l^{[i]} / \|\boldsymbol{\omega}_\sigma \boldsymbol{b}_\sigma\|_2 - \|\boldsymbol{b}_l\|_2^2\right)}, \delta = \left\|\boldsymbol{\omega}_p^{1/2} \boldsymbol{b}_p\right\|_1 + \left\|\boldsymbol{\omega}_\sigma^{1/2} \boldsymbol{b}_\sigma\right\|_2. \tag{21}$$

This part of the specific weight setting process can be found in our work in Reference [25]. The final improved SPICE update formula is obtained as

$$\sigma_l^{[i+1]} = \left\| \varphi_{L+l}^H \left(\boldsymbol{R}^{[i]}\right)^{-1} \widehat{\boldsymbol{R}}^{1/2} \right\|_1^{1/2} \|\boldsymbol{\omega}_\sigma \boldsymbol{b}_\sigma\|_2 / \omega_{L+l}^{1/2} \delta \tag{22}$$

$$p_l^{[i+1]} = \left\| \varphi_l^H \left(\boldsymbol{R}^{[i]}\right)^{-1} \widehat{\boldsymbol{R}}^{1/2} \right\|_2 / \omega_l^{1/2} \delta. \tag{23}$$

In practice, it has been found that the spatial–spectral lines obtained using this method possess smoother and sparser features, which, in the absence of a priori, effectively aids in accurately estimating the DOA of multiple sources at small angular intervals in space.

2.3. Interference Suppression Weight

After obtaining information about the direction of the sound source, suppression of the interference using spatial methods is started. In the INCM method, the correlation matrix of the signal to be suppressed can be expressed as

$$R_i = \int_{\boldsymbol{\theta}} P_{Capon}(\theta) a(\theta) a^H(\theta) d\theta \tag{24}$$

where P_{capon} is the space energy estimate of Capon's method, and $\boldsymbol{\theta}$ is the set of all angles that do not contain a SOI. In interference environments with low signal-to-noise ratios (SNRs), the interference of noise may cause the method based on this matrix reconstruction to fail. So, for this, we use the modified SPICE method to construct the ICM to exclude the noise effect. Using our method during DOA estimation, we can obtain the energy distribution in noise and energy space. Here, we assume that a certain angle $\boldsymbol{\Theta}$ among multiple sources is the direction of the target signal, and the other sources are the interfering signals. When the signal has mainlobe interference, the mainlobe interference also lies in the complement set of angular grid $\bar{\boldsymbol{\Theta}}$. Note that the set of angles formed by $\boldsymbol{\Theta}$ and $\bar{\boldsymbol{\Theta}}$ here refers to the set consisting of all targets and interference sources, and not the set of all

angles except SOI in the traditional INCM. The interference correlation matrix using $\boldsymbol{P}_s$ reconstruction can be expressed as

$$\widehat{R}_i = \sum_{\theta \in \bar{\boldsymbol{\Theta}}} \hat{P}_s(\theta) a(\theta) a(\theta)^H \tag{25}$$

where $\hat{P}_s$ is obtained through the modified SPICE. The ICM can be eigen-projection as follows:

$$\widehat{R}_i = S \Lambda S^H = \sum_{k=1}^{M} \lambda_k s_k s_k^H = S_i \Lambda_i S_i^H + S_n \Lambda_n S_n^H \tag{26}$$

where $\{\lambda_k, k = 1, \cdots, M\}$ are the descending eigenvalues of $\widehat{R}_i$, and s_k is the kth eigenvector. Assume that the number of interferences is Q. $S_i = \left[s_1, \cdots, s_{Q+1}\right]$ denotes the interference subspace and $S_n = \left[s_{Q+2}, \cdots, s_M\right]$ denotes the noise subspace. Thanks to the energy estimation during SPICE fitting, this reconstructed matrix spatially filters out a large number of noise components, and the S_n contains only a negligible amount of noise in the direction of the interference. The $\Lambda_i = \left[\lambda_1, \cdots \lambda_{Q+1}\right]$ is the diagonal array whose dimension is the number of interferences.

Next, we need to target the mainlobe interference and suppress it. The mainlobe width is fixed in small arrays with known array structures. For a uniform line array with spacing d, and assuming that the target direction is θ_0, the mainlobe width W_{ML} can be expressed as

$$W_{ML} = 2 \arcsin\left(\frac{\widehat{\lambda}}{Md} + \sin\theta_0\right) \tag{27}$$

where $\widehat{\lambda}$ is the wavelength of the signal. Thus, the mainlobe angle sector can be defined as

$$\Phi = \left(\theta_0 - \frac{W_{ML}}{2}, \theta_0 + \frac{W_{ML}}{2}\right). \tag{28}$$

The interference whose DOA of the signal is outside this interval is the sidelobe interference. Assuming that the number of sidelobe interferences is N_s, then the number of mainlobe interferences is $N_m = Q - N_s$. This will help us determine the number of mainlobe interferences under multiple interference scenarios, enabling us to suppress them in a more targeted manner. When we obtain the number of mainlobe interferences, we need to separate the feature vectors corresponding to the mainlobe interferences in the interference coherence matrix. According to Reference [24], their coherence coefficients will be larger when the interference energy's incoming angle is closer to the incoming direction of the target signal. Here, the interference eigenvector coherence coefficient is calculated as

$$\mathrm{co}(s_i, a(\theta_0)) = \frac{s_i^H a(\theta_0)}{\|s_i\| \|a(\theta_0)\|}. \tag{29}$$

The vector of mainlobe interference is satisfied as

$$\left|\mathrm{cor}(s_i, a(\theta_0))\right|_{N_m} = \max_{s_i} \left| \frac{s_i^H a(\theta_0)}{\|s_i\| \|a(\theta_0)\|} \right|_{N_m}. \tag{30}$$

Accordingly, we can then filter to get the eigenvalues λ_m and eigenvectors s_m of the mainlobe interference from $\widehat{R}_i$. Then, construct the eigen-projection matrix through a blocking masking matrix with s_m as

$$M_e = I - s_m\left(s_m^H s_m\right)^{-1} s_m^H \tag{31}$$

where I is the identity matrix. According to Reference [28], decreasing the dominant interference eigenvalue λ_m can further eliminate the apparent dominant interference. Note that setting it to zero introduces unnecessary computational problems. Therefore, before calculating the interference suppression weights, we additionally solved for the mean value λ_d of the non-interference eigenvalues, which can be obtained from the following equation:

$$\lambda_d = \frac{\lambda_{Q+1} + \lambda_{Q+2} + \cdots + \lambda_M}{M - Q}. \tag{32}$$

It should be noted that λ_d is the average of the eigenvalues of the non-interfering signals, and its physical meaning reflects the energy of the noise space. However, after the ICM reconstruction, the noise energy contained in $\widehat{R}_i$ is actually negligible due to the energy space division in improved SPICE. Therefore, compared to λ_m, the value of λ_d is very small but not equal to 0. Replacing λ_m with λ_d satisfies the need to reduce the eigenvalue of the mainlobe interference and avoids unnecessary computational problems. The reconstructed signal interference correlation matrix after the replacement is expressed as

$$R_{si} = S\hat{\Lambda}S, \hat{\Lambda} = \mathrm{diag}(\lambda_1, \cdots, \lambda_{m-1}, \lambda_d, \lambda_{m+1}, \cdots, \lambda_M). \tag{33}$$

Solve the mainlobe interference suppression adaptive weights using the above equation as

$$w = \frac{R_{si}^{-1} a(\theta_0)}{a(\theta_0)^H R_{si}^{-1} a(\theta_0)}. \tag{34}$$

Finally, bringing in Equations (31) and (34), we get the output of the adaptive mainlobe interference suppression beamformer as

$$Y_o = w^H M_e X. \tag{35}$$

The flow of the whole method is schematized in Figure 1.

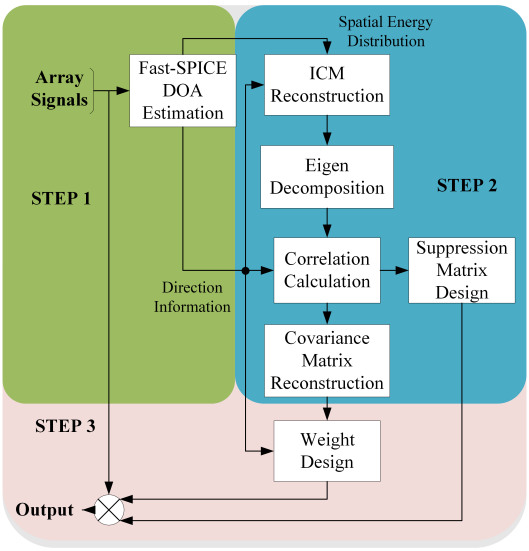


Figure 1. The flowchart of the method.

3. Simulations

All experimental simulation procedures were performed on a personal computer with 3.7 GHz Intel(R) Core(TM) i9-10900K CPU and 64 GB RAM. Lenovo China manufactured this equipment named 9000K-2021.

3.1. Simulation Setup

In the simulation experiments, we use a uniform line array of eight array elements with a spacing of 0.13 m. The sampling frequency is 32 kHz, and it is assumed that N far-field narrowband signals will be received simultaneously; one of them is the SOI and the others are interference. For all far-field sources in our simulation, we use single-frequency signals. Gaussian white noise is used to simulate the environment noise in the experiments. We assume that the DOA is uniformly discretized as a set of grids $\Theta = [\Theta_1, \Theta_2, \cdots, \Theta_L]$ with grid spacing $r = 180^\circ/\mathrm{L}$ and the number of grids $L = 200$. Each segment of the signal has 200 snapshots for algorithmic processing, and we consider that the sources incident on the array are all far-field signals. The definition of the signal-to-interference ratio (SIR) is similar to that of the SNR. When the main factor affecting signal quality in the background is not noise but interference, the SIR is usually used to evaluate signal quality. This paper uses the SIR as one of the main measurement indicators, and it can be defined as

$$\mathrm{SIR} = \hat{\sigma}_s^2 / \hat{\sigma}_i^2 \tag{36}$$

where $\hat{\sigma}_s^2$ and $\hat{\sigma}_i^2$ in the above equation denote the energy of the SOI and the energy of the interfering signal, respectively. The signal-to-interference and noise ratio (SINR) can be solved by following Equation (37), according to Reference [24].

$$\mathrm{SINR} = \frac{\hat{\sigma}_s^2 \left| w^H a(\theta_0) \right|}{w^H R_{i+n} w} \tag{37}$$

where R_{i+n} is the noise and interference correlation matrix without SOI energy. The SINR calculated in this way can effectively reflect the SOI energy loss due to the mainlobe offset in the method. It is worth noting that the mainlobe width under the 8-element array is approximately 30°. Therefore, the angular intervals between the SOI and the mainlobe interference signal randomly generated under the simulation conditions in this paper are all less than 15°.

3.2. DOA Estimation Simulation

We simulate the performance of the DOA estimation part of the algorithms. An SOI signal and an interference signal are randomly generated within −15° to 15°, and the arrival angle of the interfering signal is −2.7°, the arrival angle of the SOI is −9.9°. The energy of each interference signals in the simulation experiment is 20 dB, and the SNR of the input signal is 5 dB. The DOA estimation methods involved in the comparison are CBF, minimum variance distortionless response (MVDR) [29], multiple signal classification (MUSIC) [30], root sparse Bayesian learning (ROOT-SBL), and SPICE. The experimental results are shown in Figure 2.

Obviously, the CBF method has difficulty detecting SOIs that are swamped by the mainlobe interference. The MUSIC method produces spurious spectral peaks. The super-resolution methods, including the method in this paper, can effectively detect low-SIR SOIs. The spectral peaks formed by the method in this paper are the most obvious among them. The result demonstrates the ability of the DOA estimation method used in this paper to detect low-SIR signals in the presence of small angular intervals mainlobe interference.

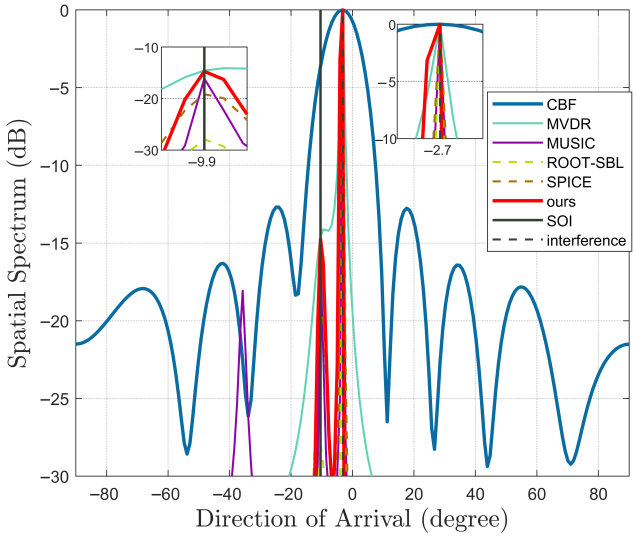


Figure 2. The DOA estimation results under one small angular interval mainlobe interference.

3.3. Interference Suppression Simulation

After proving the effectiveness of the DOA estimation method, we test the ability of present method to suppress the interference signal. It is assumed in the simulation tests in this section that the methods to be tested all obtain the correct DOA as the target beam pointing, and the gain curve is plotted at a half-wavelength frequency to verify the suppression effect.

The first simulation is the mainlobe interference suppression ability in the single mainlobe interference scenario. In this subsection, two kinds of graphs of SOI at 0° and interference signal (InS) at 0° are drawn to show the suppression ability of each method. When the SNR of the SOI is 5 dB and the SNR of the interfering signal is 15 dB, the gain of the beam under strong interference is shown in Figures 3 and 4. The iterative adaptive approach with interference and noise covariance matrix reconstruction (IAA-CMR) is the control group for the combination method of References [23,24]. It can be seen that all the methods to be tested undergo a shift of the mainlobe to suppress the mainlobe interference. Among these methods, this paper creates the deepest trapping in the direction of the interference and effectively achieves the purpose of mainlobe interference suppression.

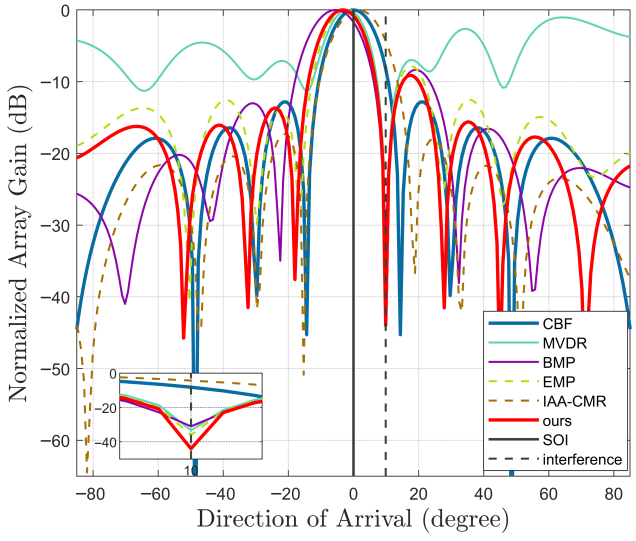


Figure 3. The beam gain with one mainlobe interference (SOI: 0°; InS: 10°).

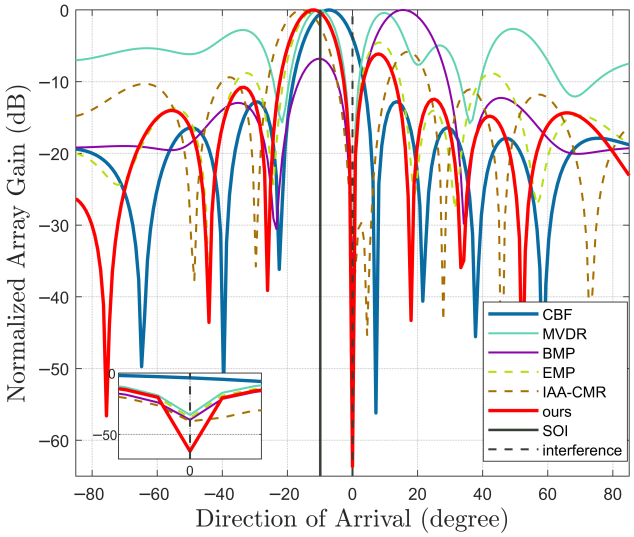


Figure 4. The beam gain with one mainlobe interference (SOI: −10°; InS: 0°).

Next, we simulate the output SIR of various methods at different angle intervals under a fixed SNR in Figure 5. The SNR of both SOI and interference is 5 dB, with SOI fixed at 0° and interference tested at different angle intervals from 0° to 20°. When the angle interval is less than 13.5°, the interference is the mainlobe interference. The curves of the methods in this paper increase steadily with the angular interval. It is worth noting that we assume that all methods obtain correct DOA estimates in this figure. However, in practice, due to the performance limitations of small arrays, angular intervals below 3° are often difficult to distinguish as two signals by DOA estimation. Hence, intervals above 3° are more informative. We calculate the average SIR improvement of all methods compared to CBF in the 3–13.5° mainlobe interference interval. The average SIR improvement is 15.59 dB for the method in this paper, 13.58 dB for the EMP method, and less than 10 dB for all other methods. In summary, the methods in this paper will outperform the other methods compared at most angular intervals.

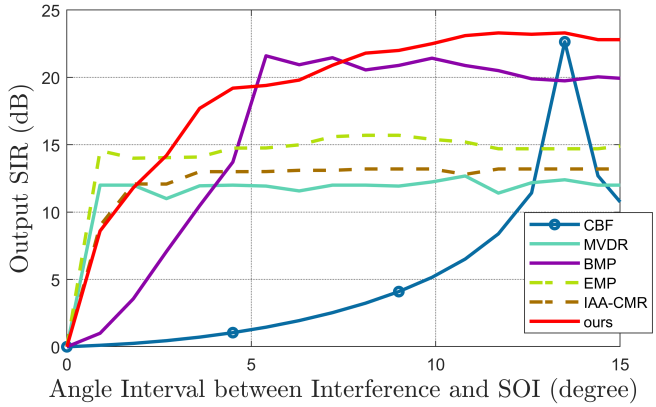


Figure 5. SIR variation curves under mainlobe interference with angle interval changed.

Figure 6 plots the output SIR versus input SIR for all test methods. We make an angular interval between the interfering signal and the SOI of 5°. Keeping the SOI signal energy constant at 5 dB, we vary the interference energy at different SIRs. Our method can provide higher SIR enhancement than other comparative methods at all SIR levels. When the input SIR is increased, the output SIR of the other methods decreases by a significant margin. This is due to their inability to provide sufficient trapping in the direction of the

weaker mainlobe interference. Thanks to the two-stage suppression, the method in this paper possesses stronger interference capability, whether the interference energy is weak or strong.

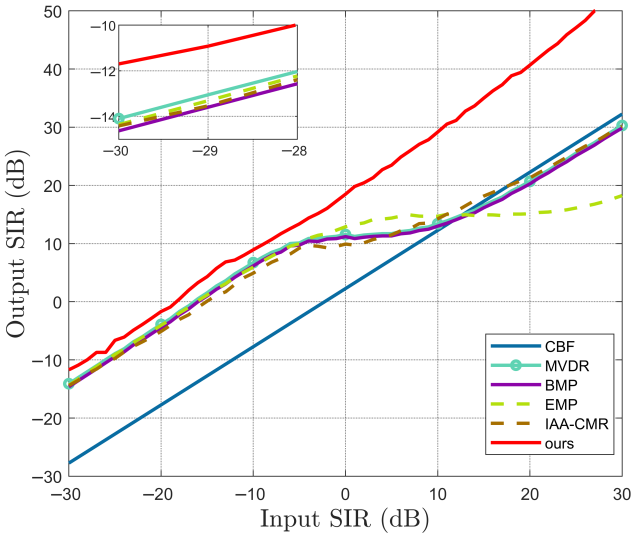


Figure 6. The SIR variation curves under mainlobe interference with a fixed incident angle.

Figure 7 shows the SINR curves using the calculation method presented in the previous section. The figure reflects the mainlobe offset for each mainlobe interference suppression method. The ideal output in the figure is the SINR when the mainlobe is fully aligned with the SOI direction. It can be seen that the method in this paper actually sacrifices a certain amount of mainlobe offset for deeper trapping in order to improve the suppression ability of mainlobe interference. However, unlike the curve trend of other methods, the main-valve offset of this paper's method is controlled within a certain range at each input SIR level, and there is no excessive loss of gain in the SOI direction.

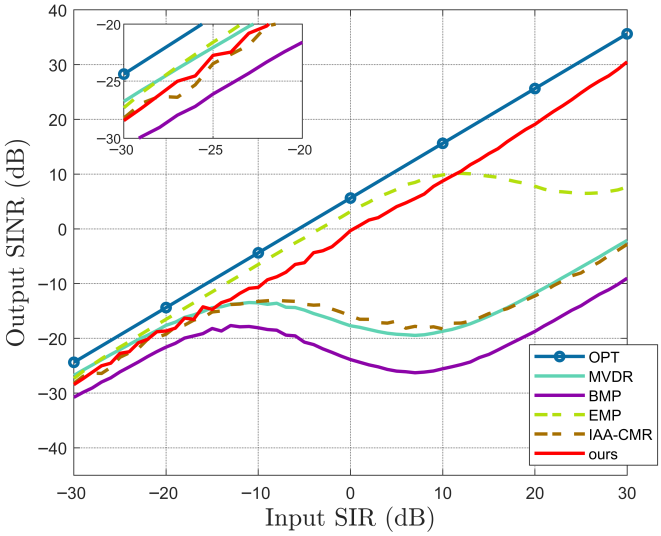


Figure 7. The SINR variation curves under mainlobe interference with a fixed incident angle.

Next we discuss each method's mainlobe interference rejection capability in the same way for the case of mainlobe and sidelobe interference coexistence. Three sources were generated between $-15°$ and $60°$ on the grid randomly, with SOI at a DOA of $-9.9°$, and the mainlobe and sidelobe interference at $-2.7°$ and $56.7°$. The signal energies are

5 dB, 15 dB and 15 dB, respectively. Figure 8 shows the normalized gain curves of each method. It can be seen that this paper's method can form the deepest trapping at the mainlobe interference and the sidelobe interference, and the mainlobe offset is also within a reasonable range. This proves that the present method still has an effective interference suppression capability in the scenario of mainlobe and sidelobe coexistence, and the SOI energy loss brought by the mainlobe offset is within an acceptable range.

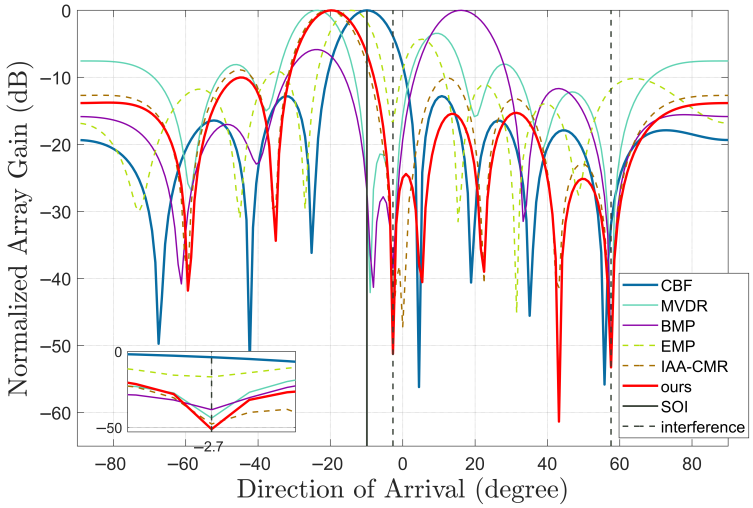


Figure 8. The beam gain with mainlobe interference and sidelobe interference.

Figure 9 shows a control variable experiment aimed at verifying the contribution of each component of the method in this paper to the SIR boosting effect. The angle interval in the simulation is 10° and the SNR of SOI is 5 dB. BM denotes the blocking masking matrix, EP denotes eigen-projection, and I and IN denote ICM and INCM, respectively. The masking matrix provides more SIR gain in the low-SIR case. In contrast, using the interference matrix reconstruction instead of the noise interference matrix increases the stability of the output gain at each input SIR level. It increases the suppression of weak interference in the high-SIR case.

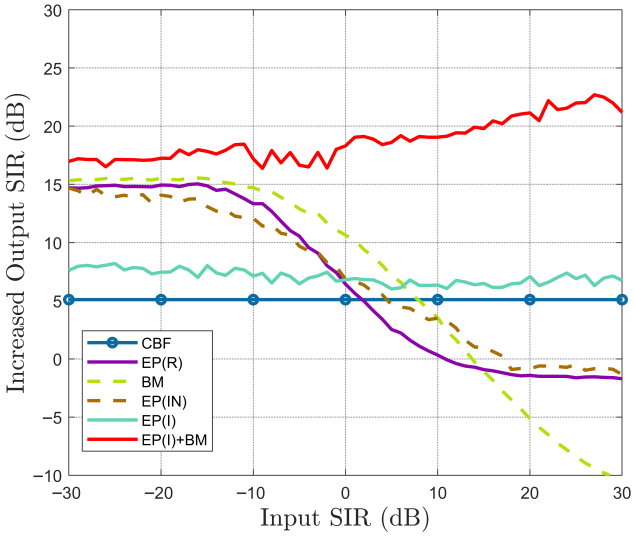


Figure 9. The contribution of the components to the SIR performance improvement in this paper.

We conducted simulation experiments to simulate real scenarios and test several complete system methods with DOA estimation and mainlobe suppression capabilities.

A modulated sine wave is used as the SOI, and white noise is used as the interfering signal. The SNR for SOI and interference is 5 dB, and the angle interval is 10°. The interference suppression beamforming methods are compared by their own DOA estimation results, and the experimental results of the time-domain waveforms are shown in Figure 10. It can be seen that the CBF method does not face mainlobe interference with any interference suppression capability due to the mainlobe pointing in the direction of the interference. The other three methods have some interference suppression ability. After calculation, the output SIRs of the MVDR and IAA-CMR methods are 13.29 dB and 14.74 dB, respectively. The output SIR of the method in this paper is 22.88 dB, which confirms our method's better mainlobe interference suppression ability.

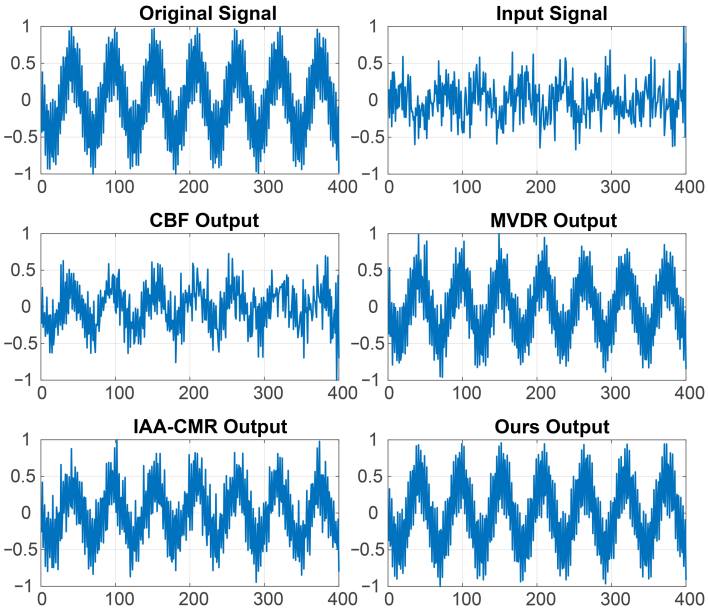


Figure 10. The simulation results of the time-domain waveforms.

Finally, the computational efficiency of this method is discussed. Under the above simulation conditions, the processing time of this method is 471.5 ms for a section of signal with a length of 1 s and a sampling frequency of 32 K, including 269.34 ms for high-precision DOA estimation and 202.16 ms for interference suppression beamforming. This method can perform real-time processing, and the calculation speed should be improved on a better computing platform.

4. Results

This section evaluates the performance of the methods in this paper using real experimental data. The experimental scenario was somewhat introduced in our previous paper [25], and its general scenario is shown in Figure 11.

The experiments were carried out in a sea area in the South China Sea, and the experimental data was collected using a horizontal uniform linear array (ULA) deployed at a depth of 15 m. For the sensor part, we used the BK8105 commercial hydrophones. They have a sensitivity of -205 ± 2 dB re 1 V/μPa and a frequency response of $+1/-6.5$ dB from 0.1 Hz to 100 kHz. The array consists of eight receivers, which are spaced 13 cm apart as in Figure 12. A small engineering vessel is used as a real target, and the interference acoustic source is fixed at a depth of 10 m, broadcasting continuous broadband noise. The experiment started with the target sailing in a direction away from the receiver array. In data processing, we chose to intercept a section of the data in which the SIR was lower and the DOA interval was smaller to verify the mainlobe interference suppression effect.

We chose to use seven consecutive channels of data for the study because fewer arrays with wider mainlobe widths better reflect the performance of the mainlobe interference suppression algorithm. Narrowband data centered on the array half-wavelength frequency is intercepted to construct the covariance matrix, which is constructed based on 200 snapshots. The initial parameter settings for all the methods are the same as the simulation experiment settings in Section 3.

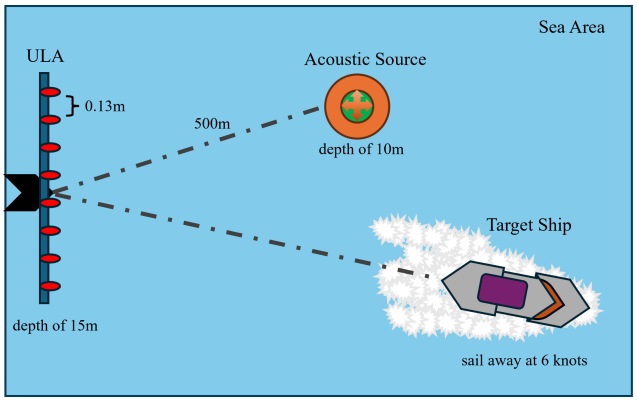


Figure 11. The schematic of the experiment.

Then, the beamforming test is performed for all mainlobe interference suppression methods using the actual DOA values. Figure 13 shows the true normalized gain plot at that moment. The BMP and EMP methods do not form effective traps, the IAA-CMR method forms a false gain peak in the direction of the interference, and the MVDR method does not have a sufficient trap. The method proposed in this paper achieves the maximum trapping gain for mainlobe interference, thereby demonstrating its effectiveness in suppressing such interference.

Figure 14 shows the experimental data gain history for each method, where the red line indicates the target track and the orange dashed line indicates the interference track. The greener the color of the graph, the stronger the gain in the corresponding direction, and the bluer the color of the graph, the stronger the suppression effect. It can be clearly seen that among the compared methods, only the method in this paper generates a stable strong suppression trap in the interference direction while maintaining the target gain. All other methods are limited by the width of the mainlobe which cannot generate effective suppression traps, fully proving the method's effectiveness in this paper.

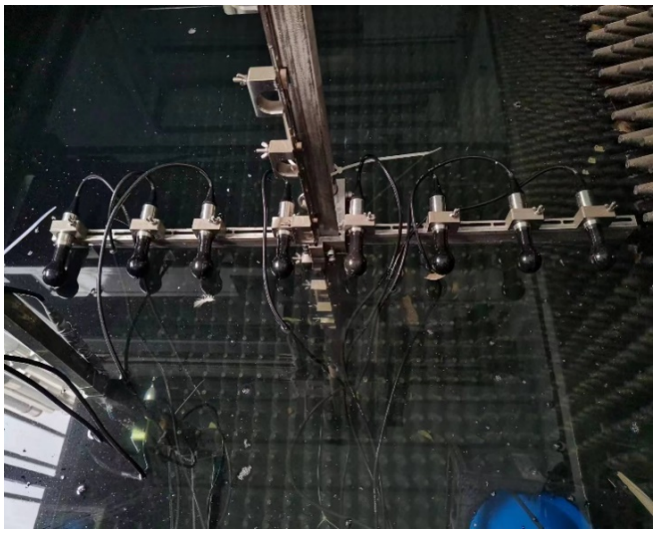


Figure 12. The hydrophone array used in the experiment.

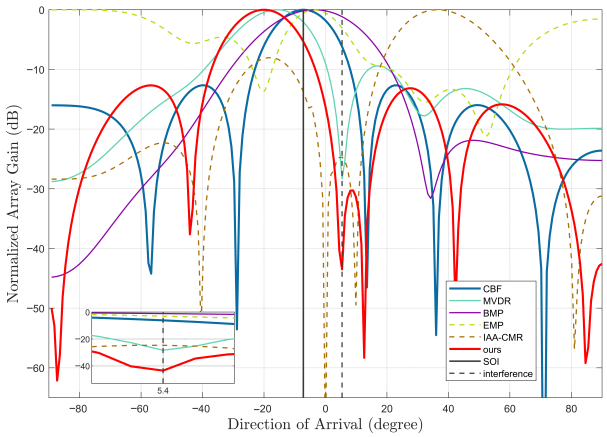


Figure 13. The beam gain in the experiment at a random moment.

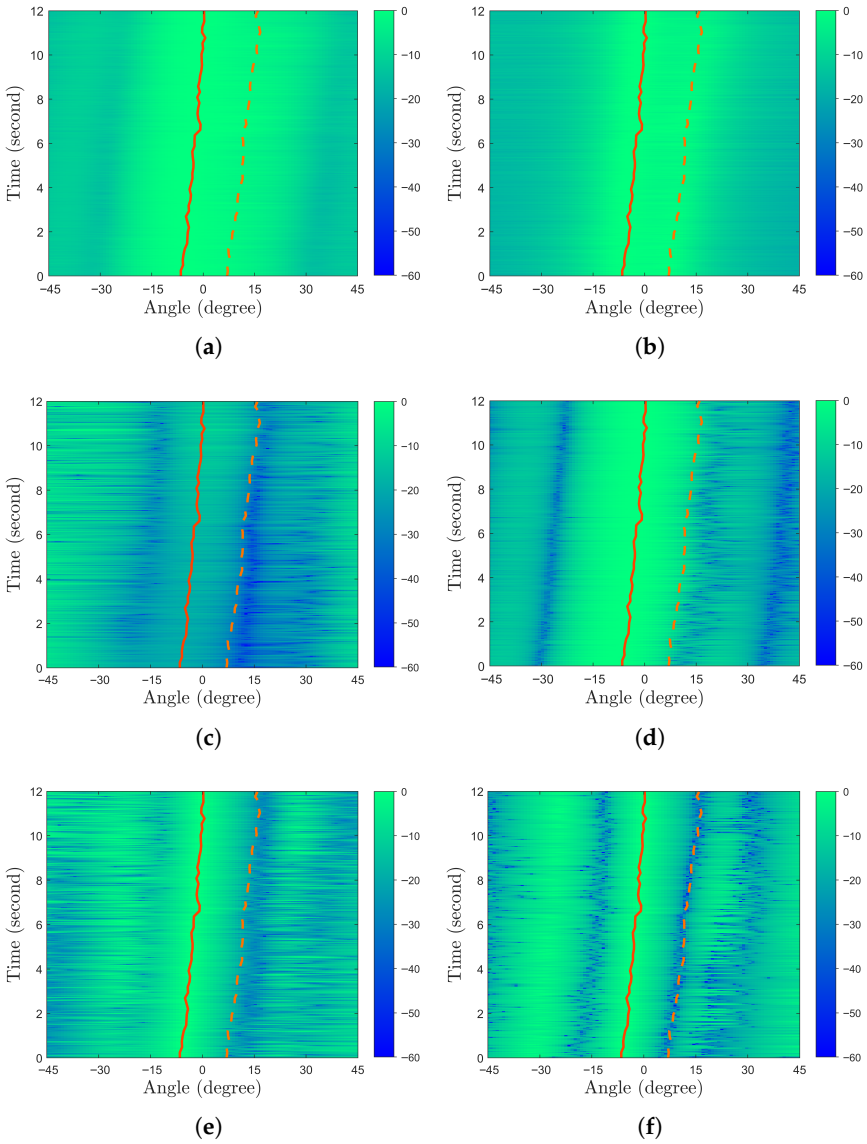


Figure 14. The experimental data gain history for each method (the red line indicates the target track, and the orange dashed line indicates the interference track). (**a**) CBF; (**b**) MVDR; (**c**) BMP; (**d**) EMP; (**e**) IAA-CMR; (**f**) Method in this paper.

5. Discussion

The mainlobe interference suppression capability of the method in this paper is confirmed through simulation and experimental tests. The DOA estimation method adopted in the first part of this paper can accurately provide super-resolution DOA estimation capability in the case of wide main flap, and usually in real application scenarios, the angular differentiation limit of the DOA estimation performance of the experimental small and medium-sized arrays is roughly 3°, which is much better than that of the traditional DOA estimation method. Within the mainlobe interference interval angle of 3° to 13.5° from SOI based on eight-element uniform linear arrays, the method in this paper can enhance the SIR by about 15.59 dB on average, compared with the interference-free suppression of CBF, and outperforms the other interference suppression methods simultaneously. In the ablation experiments, we analyze the effects of EMP and BMP on interference suppression, and the two-stage mask suppression method combining them has a significant suppression improvement. The improved ICM reconstruction can better avoid noise interference in lower-SNR scenarios compared to INCM. In the real test environment, the interference suppression provided by this paper performs very well compared to the comparison methods. On the other hand, feature decomposition is used in this paper's method, and it is possible that coherent interference signals may adversely affect the suppression effect. Furthermore, it remains to be tested whether the method can adapt to the interference suppression in wideband signal processing scenarios. These two points are the next step of the team's work.

6. Conclusions

This paper uses an adaptive mainlobe interference suppression method to enhance the signal-to-interference ratio of small array beamforming. To solve the problem of difficult suppression of interference at small angular intervals due to the large mainlobe width limited by physical dimensions, an improved spatial fitting method is first used to provide an accurate DOA estimation with super-resolution. Then, the energy distribution matrix obtained during the fitting process is utilized to reconstruct the interference coherence matrix. Finally, the reconstructed interference coherence matrix is used to construct a blocking masking matrix and the eigen-projection matrix to suppress the mainlobe interference signal. This method effectively solves the problem of difficulty suppressing the mainlobe interference of small aperture arrays. In simulation experiments, the method in this paper can better suppress mainlobe interference. Within the mainlobe interference interval angle of 3° to 13.5° from SOI based on eight-element uniform linear arrays, the method in this paper can enhance the SIR by about 15.59 dB on average compared with the interference-free suppression of CBF. In field experiments, this paper's method also has a pronounced effect on the strong mainlobe interference signal suppression, which proves the adaptive ability and interference suppression ability of this paper's method in small sonar arrays for complex detection environments.

Author Contributions: Methodology, W.W.; Software, W.W.; Resources, Y.L.; Data curation, T.S.; Writing—original draft, W.W.; Visualization, L.M.; Project administration, Y.L. and D.Z.; Funding acquisition, D.Z. All authors have read and agreed to the published version of the manuscript.

Funding: This research received no external funding.

Data Availability Statement: The datasets presented in this article are not readily available because access rights belong to the author's institution. Requests to access the datasets should be directed to zdx_3s@163.com.

Conflicts of Interest: The authors declare no conflicts of interest.

Abbreviations

The following symbols and abbreviations are used in this manuscript:

Symbol	Meaning	Symbol	Meaning
$E\{\cdot\}$	Expectation operator	$\mathrm{tr}(\boldsymbol{A})$	The trace of the matrix $\boldsymbol{A}$
$\boldsymbol{A}^H$	Hermite transpose of $boldsymbol A$	$\max(\cdot)$	Maximum value operator
$\boldsymbol{A}^{-1/2}$	Hermitian positive definite square root of $\boldsymbol{A}^{-1}$	$\lvert\cdot\rvert$	Calculate the absolute value
$\lVert\cdot\rVert_2$	L2 norm	$\mathrm{diag}(a,b)$	Construct a diagonal matrix using a, b
$\lVert\cdot\rVert_1$	L1 norm	$\mathrm{co}(a,b)$	Coherence coefficient of a and b
Abbreviation	**Definition**	**Abbreviation**	**Definition**
AUV	autonomous underwater vehicle	BMP	blocking matrix preprocessing
CBF	conventional beamforming	CMR	covariance matrix reconstruction
DOA	direction of arrival	EMP	eigen-projection matrix preprocessing
IAA	iterative adaptive approach	ICM	interference coherence matrix
INCM	interference and noise covariance matrix	MVDR	minimum variance distortionless response
MUSIC	multiple signal classification	SBL	sparse Bayesian learning
SOI	signal of interest	SIR	signal-to-interference ratio
SINR	signal-to-interference and noise ratio	SNR	signal-to-noise ratio
SPICE	sparse iterative covariance-based	ULA	uniform linear array

References

1. Ma, T.; Ding, S.; Li, Y.; Fan, J. A review of terrain aided navigation for underwater vehicles. *Ocean Eng.* **2023**, *281*, 114779. [CrossRef]
2. Wang, F.-Q.-W.; Zhang, X.; Xing, X.-F.; Zhang, X.-J. The Research of Underwater Acoustic Detection System for Small AUV. In Proceedings of the 2015 Fifth International Conference on Instrumentation and Measurement, Computer, Communication and Control (IMCCC), Qinhuangdao, China, 18–20 September 2015; pp. 1828–1831.
3. Maguer, A.; Dymond, R.; Grati, A.; Stoner, R.; Guerrini, P.; Troiano, L.; Alvarez, A. Ocean gliders payloads for persistent maritime surveillance and monitoring. In Proceedings of the 2013 OCEANS, San Diego, CA, USA, 23–27 September 2013.
4. Zhang, Z.; Lin, M.; Li, D.; Wu, R.; Lin, R.; Yang, C. An AUV-Enabled Dockable Platform for Long-Term Dynamic and Static Monitoring of Marine Pastures. *IEEE J. Ocean. Eng.* **2025**, *50*, 276–293. [CrossRef]
5. Zhang, M.; Tong, F.; Zhang, F.; Wei, B. CoralBuddy-1: A Micro-Sized Autonomous Underwater Vehicle for Offshore Coral Reef Monitoring. In Proceedings of the 17th International Conference on Underwater Networks & Systems, New York, NY, USA, 24–26 November 2023. [CrossRef]
6. Hirotsu, R.; Ura, T.; Kojima, J.; Sugimatsu, H.; Bahl, R.; Yanagisawa, M. Classification of sperm whale clicks and triangulation for real-time localization with SBL arrays. In Proceedings of the OCEANS 2008, Quebec City, QC, Canada, 15–18 September 2008; p. 553.
7. Wolek, A.; McMahon, J.; Dzikowicz, B.R.; Houston, B.H. Tracking Multiple Surface Vessels With an Autonomous Underwater Vehicle: Field Results. *IEEE J. Ocean. Eng.* **2022**, *47*, 32–45. [CrossRef]
8. Chun, S.; Kawamura, C.; Ohkuma, K.; Maki, T. 3D Detection and Tracking of a Moving Object by an Autonomous Underwater Vehicle with a Multibeam Imaging Sonar: Toward Continuous Observation of Marine Life. *IEEE Robot. Autom. Lett.* **2024**, *9*, 3037–3044. [CrossRef]
9. Glegg, S.A.L.; Olivieri, M.P.; Coulson, R.K.; Smith, S.M. A Passive Sonar System Based on an Autonomous Underwater Vehicle. *IEEE J. Ocean. Eng.* **2002**, *26*, 700–710. [CrossRef]
10. Chi, C.; Pallayil, V.; Chitre, M. Design of an adaptive noise canceller for improving performance of an autonomous underwater vehicle-towed linear array. *Ocean Eng.* **2016**, *202*, 106886. [CrossRef]
11. Xu, Y.; Kong, X.; Cai, Z. Cross-validation strategy for performance evaluation of machine learning algorithms in underwater acoustic target recognition. *Ocean Eng.* **2024**, *299*, 117236. [CrossRef]
12. Li, J.; Tong, F.; Zhou, Y.; Yang, Y.; Hu, Z. Small Size Array Underwater Acoustic DOA Estimation Based on Direction-Dependent Transmission Response. *IEEE Trans. Veh. Technol.* **2022**, *71*, 12916–12927. [CrossRef]
13. Aldeman, M.R. A hybrid spiral microphone array design for performance and portability. *Appl. Acoust.* **2020**, *170*, 107512. [CrossRef]

14. Stoica, P.; Babu, P.; Li, J. SPICE: A Sparse Covariance-Based Estimation Method for Array Processing. *IEEE Trans. Signal Process.* **2011**, *59*, 629–638. [CrossRef]
15. Stoica, P.; Babu, P. SPICE and LIKES: Two hyperparameter-free methods for sparse-parameter estimation. *Signal Process.* **2012**, *92*, 1580–1590. [CrossRef]
16. Zhang, J.; Qu, H.; Li, R.; Chen, C.; Chen, W. Fast 2D Weighted Generalized Sparse Iterative Covariance-Based Estimation for Scanning Radar. *IEEE Signal Process. Lett.* **2025**, *32*, 2364–2368. [CrossRef]
17. Dai, J.; Bao, X.; Xu, W.; Chang, C. Root Sparse Bayesian Learning for Off-Grid DOA Estimation. *IEEE Signal Process. Lett.* **2016**, *24*, 46–50. [CrossRef]
18. Liang, Y.; Zheng, X.; Meng, W.; Li, J.; Chen, F. Noise Integral-Based Sparse Bayesian Learning for DOA Estimation Using Grid Pruning and Adaptation. *Electron. Lett.* **2025**, *61*, e70325. [CrossRef]
19. Xing, C.; Wu, Y.; Xie, L.; Zhang, D. A sparse dictionary learning-based denoising method for underwater acoustic sensors. *Appl. Acoust.* **2021**, *180*, 108140. [CrossRef]
20. Qian, J.; He, Z.; Jia, F.; Zhang, X. Mainlobe interference suppression in adaptive array. In Proceedings of the 2016 IEEE 13th International Conference on Signal Processing (ICSP), Chengdu, China, 6–10 November 2016; pp. 470–474. [CrossRef]
21. Ma, X.; Jiang, S.; Zhang, S.; Zhang, R.; Sheng, W. Joint Wideband Beamforming Algorithm for Main Lobe Jamming Suppression in Distributed Array Radar. *Remote Sens.* **2024**, *16*, 2402. [CrossRef]
22. Han, B.; Yang, X.; Lv, Q.; Li, W.; Zhang, Z.; Zhong, S. Mainlobe and sidelobe jamming suppression method based on distributed array radar with eigen-projection matrix processing and null constraints. *IET Radar Sonar Navig.* **2024**, *18*, 2212–2221. [CrossRef]
23. Gu, Y.; Leshem, A. Robust Adaptive Beamforming Based on Interference Covariance Matrix Reconstruction and Steering Vector Estimation. *IEEE Trans. Signal Process.* **2012**, *60*, 3881–3885. [CrossRef]
24. Wang, Y.; Bao, Q.; Chen, Z. Robust mainlobe interference suppression for coherent interference environment. *EURASIP J. Adv. Signal Process.* **2016**, *2016*, 135. [CrossRef]
25. Wang, W.; Li, Y.; Shen, T.; Liu, F.; Zhao, D. An effective DOA estimation method for low SIR in small-size hydrophone array. *Appl. Acoust.* **2024**, *217*, 109848. [CrossRef]
26. Ottersten, B.; Stoica, P.; Roy, R. Covariance Matching Estimation Techniques for Array Signal Processing Applications. *Digit. Signal Process.* **1998**, *8*, 185–210. [CrossRef]
27. Stoica, P.; Zachariah, D.; Li, J. Weighted SPICE: A unifying approach for hyperparameter-free sparse estimation. *Digit. Signal Process.* **2014**, *33*, 1–12. [CrossRef]
28. Li, R.F.; Wang, Y.L.; Wan, S.H. Robust adaptive beam forming under main lobe interference conditions. *Syst. Eng. Electron.* **2002**, *24*, 61–64.
29. Zhou, J.; Bao, C.; Jia, M.; Xiong, W. A distortionless convolution beamformer design method based on the weighted minimum mean square error for joint dereverberation and denoising. *Speech Commun.* **2024**, *158*, 103054. [CrossRef]
30. Pan, Y.; Zhang, L.; Xu, L.; Duan, F. DOA Estimation on One-Bit Quantization Observations through Noise-Boosted Multiple Signal Classification. *Sensors* **2024**, *24*, 4719. [CrossRef]

Disclaimer/Publisher's Note: The statements, opinions and data contained in all publications are solely those of the individual author(s) and contributor(s) and not of MDPI and/or the editor(s). MDPI and/or the editor(s) disclaim responsibility for any injury to people or property resulting from any ideas, methods, instructions or products referred to in the content.